

# High-Resolution Monitoring of Controlled Water Table Variations From Dense Seismic-Noise Acquisitions

T. Gaubert-Bastide, S. Garambois, Clarisse Bordes, C. Voisin, L. Oxarango, Daniel Brito, P. Roux

▶ **To cite this version:**

T. Gaubert-Bastide, S. Garambois, Clarisse Bordes, C. Voisin, L. Oxarango, et al.. High-Resolution Monitoring of Controlled Water Table Variations From Dense Seismic-Noise Acquisitions. Water Resources Research, 2022, 58, 10.1029/2021WR030680 . insu-03859266

**HAL Id: insu-03859266**

**https://insu.hal.science/insu-03859266**

Submitted on 18 Nov 2022

**HAL** is a multi-disciplinary open access archive for the deposit and dissemination of scientific research documents, whether they are published or not. The documents may come from teaching and research institutions in France or abroad, or from public or private research centers.

L'archive ouverte pluridisciplinaire **HAL**, est destinée au dépôt et à la diffusion de documents scientifiques de niveau recherche, publiés ou non, émanant des établissements d'enseignement et de recherche français ou étrangers, des laboratoires publics ou privés.



Distributed under a Creative Commons Attribution - NonCommercial - ShareAlike 4.0 International License

Check for updates

AGU ADVANCING EARTH AND SPACE SCIENCE

Water Resources Research®

RESEARCH ARTICLE
10.1029/2021WR030680

# High-Resolution Monitoring of Controlled Water Table Variations From Dense Seismic-Noise Acquisitions

**T. Gaubert-Bastide[1,2], S. Garambois[2], C. Bordes[1], C. Voisin[2], L. Oxarango[3], D. Brito[1], and P. Roux[2]**

[1]Université de Pau et des Pays de l'Adour, E2S UPPA, CNRS, Total, LFCR, Pau, France, [2]Université Grenoble Alpes, CNRS, IRD, Université Savoie Mont-Blanc, Isterre, Grenoble, France, [3]Université Grenoble Alpes, CNRS, IRD, G-INP, IGE, Grenoble, France

**Key Points:**

- The use of a dense seismic network allows us to obtain high resolution dynamic maps of water content changes through a tomography process
- The space and time evolution of an hydraulic dome artificially formed under an infiltration basin is highlighted
- The obtained seismic velocity variations are sensitive to the water table fluctuations and to residual water saturation changes within the unsaturated zone

**Supporting Information:**

Supporting Information may be found in the online version of this article.

**Correspondence to:**

T. Gaubert-Bastide and S. Garambois, thomas.gaubert-bastide@univ-pau.fr; Stephane.Garambois@univ-grenoble-alpes.fr

**Citation:**

Gaubert-Bastide, T., Garambois, S., Bordes, C., Voisin, C., Oxarango, L., Brito, D., & Roux, P. (2022). High-resolution monitoring of controlled water table variations from dense seismic-noise acquisitions. *Water Resources Research*, *58*, e2021WR030680. https://doi.org/10.1029/2021WR030680

Received 24 JUN 2021
Accepted 19 JUL 2022

**Author Contributions:**

**Conceptualization:** S. Garambois, C. Bordes
**Formal analysis:** S. Garambois, C. Bordes, L. Oxarango
**Funding acquisition:** S. Garambois, C. Bordes, C. Voisin, P. Roux

© 2022. The Authors.
This is an open access article under the terms of the Creative Commons Attribution-NonCommercial-NoDerivs License, which permits use and distribution in any medium, provided the original work is properly cited, the use is non-commercial and no modifications or adaptations are made.

**Abstract** Water-resource management has become a major global issue in a world threatened by climate change. High-resolution geophysical methods may be of valuable help in monitoring the water masses, both in space and time. Passive seismic interferometry takes advantage of ambient seismic noise to recover the variations in seismic wave velocity induced by changes in groundwater. We present hereafter the time and space monitoring of an hydraulic dome artificially formed to prevent biological and chemical pollutants from entering the exploitation field of Crépieux-Charmy (Lyon, France). We use a dense seismic network to passively monitor the water table changes induced by infilling of an infiltration basin at the water supply facility for the two million inhabitants of the Lyon Metropolis (France). We assess the hourly seismic velocity variations over 19 days, during which two filling and drainage cycles were performed. The use of a dense three-component seismic network allows fine characterization of the seismic wavefield, and offers the possibility to include the analysis of 4,851 raypaths in a robust inversion algorithm based on ray theory. The velocity variations are mapped with high resolution. They are directly related to the water table variations and to residual water saturation changes within the unsaturated zone. This seismic experiment highlights the three-dimensional (3D) implementation and evolution of a hydraulic dome under the infiltration basin. This dynamic information helps in the understanding and modeling of water flows between the water table and a river, which represents a fundamental issue for discussions on the effectiveness of the barrier.

**Plain Language Summary** Monitoring aquifers becomes a crucial necessity to keep the water resource safe and sustainable, especially in water catchment fields which are usually located in proximity of urban areas. Passive seismic interferometry, which takes advantage of the continuous ambient seismic noise signals, can provide access to the properties and evolution of the water table with a noticeable spatial resolution. Here, we propose the use of a dense seismic network to monitor water content changes, artificially generated by controlled infilling/drainage cycles of a basin originally designed to mitigate potential pollution of the water field from surrounding rivers. The analysis of waves propagating within the network allows us to obtain hourly time-lapse seismic velocity variation maps with high resolution. It notably highlights the shape of a water dome that appears (or disappears) when filling (or emptying) the basin, but also that seismic variations are sensitive to both water table and water content variations occurring within the vadose zone. This study eventually shows that the seismic-noise based method can provide relevant information on fluid flow variations and pragmatically on the effectiveness of the infiltration basin to protect the water field from potential pollution.

## 1. Introduction

Unconfined aquifers are an essential water resource. Their preservation in terms of both quantity and quality is a major challenge due to the expected impacts of climate change and their exploitation by human activities. Among others, managed aquifer recharge (MAR) is a practice of increasing interest which is commonly applied to storm-water management in urban areas (Machiwal et al., 2018; Zhang et al., 2020) or water reuse (Zhang et al., 2020). Using infiltration basins or trenches, MAR systems could generate very dynamic responses of the water table and generally rely on the vadose zone for contaminant mitigation. The characterization and temporal monitoring of such systems are classically based on piezometric measurements, which provide unmatched sensitivity to water table fluctuations. However, it is by essence local and sparse due to drilling costs. Available methods for moisture and water potential monitoring based on Time Domain Reflectometry (TDR) or capacitance probes, tensiometers



19447973, 2022, 8, Downloaded from https://agupubs.onlinelibrary.wiley.com/doi/10.1029/2021WR030680 by Cochrane France, Wiley Online Library on [18/11/2022]. See the Terms and Conditions (https://onlinelibrary.wiley.com/terms-and-conditions) on Wiley Online Library for rules of use; OA articles are governed by the applicable Creative Commons License

**Methodology:** S. Garambois, C. Bordes, C. Voisin
**Project Administration:** S. Garambois, C. Bordes, D. Brito, P. Roux
**Resources:** S. Garambois, C. Voisin
**Software:** C. Voisin
**Supervision:** S. Garambois, C. Bordes
**Validation:** S. Garambois, C. Bordes
**Visualization:** S. Garambois, C. Bordes
**Writing – original draft:** S. Garambois, C. Bordes
**Writing – review & editing:** S. Garambois, C. Bordes, C. Voisin, L. Oxarango, D. Brito, P. Roux

or neutron logging face similar limitations and are generally complex to implement and maintain during long periods (Vereecken et al., 2008).

Geophysical methods can offer a wide range of characterization possibilities, which depend on their sensitivities to the physicochemical parameters of the medium, their resolution, and the depth of penetration. In appropriate conditions, they could provide a spatialization at larger scale of some hydrological variables of interest. For more than 20 years, the application and development of water-sensitive methods have been the subject of focused research referred as hydrogeophysics (Hubbard & Rubin, 2005; Rubin & Hubbard, 2006). However, depending on the scale of the studied processes, the potential for their deployment and autonomy might be a hindrance, particularly when monitoring is required with methods based on active sources (Binley et al., 2015).

Passive seismic methods such as ambient noise cross-correlation use stand-alone recording stations and benefit from continuous seismic noise sources. This continuity allows seismic wavefields to be reconstructed and then analyzed over time. Since its initial development about 20 years ago, this popular approach is increasingly used in various Earth studies for both imaging and monitoring purposes that are carried out at various scales (Campillo & Paul, 2003; Derode et al., 2003; Lobkis & Weaver, 2001). Ambient noise cross-correlation is based on the principle that cross-correlation of two seismic noise records acquired by two sensors can provide the Earth response to perturbations between the two sensors, that is, the Green's function, if the noise sources are spread isotropically in space. Basically, it means that the cross-correlation of the ambient noise recorded by two receivers is mathematically equivalent to the signal recorded by one receiver when a local source is located at the other. When continuously recorded, the ambient noise has therefore the ability to reveal any modification in medium properties, whether mechanical or hydrological, with a given temporal resolution.

This methodology has paved the way for continuous temporal monitoring of Green's functions, and in particular, to track very fine seismic velocity variations related to changes in different properties of the medium. These analyses are generally based on coda waves, which arrive in the seismic wave train that follows the ballistic waves. They represent backscattered waves from numerous heterogeneities distributed along the wave's pathway and provide very repeatable waveforms with noticeable weak variations in seismic velocities (Grêt et al., 2006). This approach was used, for instance, at the Earth crust scale to observe weak water table variations for Merapi volcano (Sens-Schönfelder & Wegler, 2006), for crustal stress reductions after a major seismic event (Wegler et al., 2009) and for fluid flow during volcano eruptions (Brenguier et al., 2011; Mordret et al., 2010). In the critical zone, various environmental processes have been monitored (Larose et al., 2015, for a review), including permafrost (James et al., 2019), water resources (Clements & Denolle, 2018; Lecocq et al., 2017), and groundwater flow (Grobbe et al., 2021).

Contrary to coda waves, which sample a tortuous path between two seismic stations many times, ballistic waves are supposed to propagate along a direct pathway between the two sensors. They can be associated to volume (P/S) or surface waves (Rayleigh/Love modes) and are identified as early arrivals in seismograms. The latter dominate the seismograms, especially in sedimentary environments where coda waves have low energy because of weak scattering potential. Recently, Voisin et al. (2017); Garambois et al. (2019) and Kim and Lekic (2019) suggested the use of ballistic waves to monitor near-surface water table variations. They were notably able to exploit and quantify the sensitivity of body and surface waves to changes in water content. However, they simply considered water table changes, without taking into account potential variations occurring within the unsaturated zone. Takano et al. (2020) also used ballistic waves to monitor an active volcano, while Brenguier et al. (2020) succeeded in separating body waves from surface waves by taking advantage of a dense seismic network.

Besides well established imaging techniques based on noise analysis, the spatialization of the observed variations is generally limited due to the sparse number of stations available. Here we show that high-resolution seismic noise interferometry can be obtained for monitoring hydrological variations. For this purpose, we deployed a network of 99 3-component (3C) seismic stations around an infiltration basin that was designed to provide an artificial recharge of the aquifer and generate a hydraulic barrier to protect the pumping wells in case of accidental pollution of surrounding rivers. After presenting the site and the sequence of filling/emptying of the basin that was monitored over 19 days, we show the global seismic processing workflow that leads to the reconstruction and analysis of 4,851 seismic traces. The dense three-component seismic network allows precise characterization and monitoring of both the noise sources and the seismic wavefield. From the analysis of the Love wave velocity variations, we reconstruct hourly tomographic images of the velocity variations with high resolution. They show,



19447973, 2022, 8, Downloaded from https://agupubs.onlinelibrary.wiley.com/doi/10.1029/2021WR030680 by Cochrane France, Wiley Online Library on [18/11/2022]. See the Terms and Conditions (https://onlinelibrary.wiley.com/terms-and-conditions) on Wiley Online Library for rules of use; OA articles are governed by the applicable Creative Commons License

19447973, 2022, 8, Downloaded from https://agupubs.onlinelibrary.wiley.com/doi/10.1029/2021WR030680 by Cochrane France, Wiley Online Library on [18/11/2022]. See the Terms and Conditions (https://onlinelibrary.wiley.com/terms-and-conditions) on Wiley Online Library for rules of use; OA articles are governed by the applicable Creative Commons License

in particular, the hydraulic dome geometry, its evolution over time and space, highlighting the effectiveness of the system in reducing water exchange between the river and the water field. In addition, this study shows that the unsaturated zone has a direct influence in the measured seismic velocity changes.

## 2. Seismic-Noise Survey of the Crépieux-Charmy Water-Catchment Field

### 2.1. A Strategic and Sensitive Site

The Crépieux-Charmy drinking water pumping field (Figure 1) is a complex system that supplies 87% of the tap water for the two million inhabitants of the Lyon metropolitan area (France). It extends to the East of Lyon over a highly protected area of 375 ha, where 111 wells pump the groundwater into the modern fluvial aquifer. This strategic area located in the vicinity of a highly urbanized area and surrounded by rivers and canals, is very sensitive to pollution risks, especially from rivers. To protect groundwater from river pollution and maintain the groundwater level, 12 infiltration basins were built around the pumping areas. These infiltration basins are filled with a 50 cm thick sand layer for filtration purposes. A previous study put forward the major role of a compacted soil layer beneath the sand probably due to the basin construction work (Réfloch et al., 2017). It limits the infiltration rate and contributes maintain an unsaturated layer between the basin and the water table. The basin is supplied from a pumping system fed by a sedimentation basin connected to the Vieux Rhone river (Figure 1b). The pumping system is controlled to maintain a maximum head of 1.8 m in the basin with 0.2 m fluctuations (Figure 1c) and a minimum vadose zone thickness of 2 m below the basin. Moreover, the pumping stops if the turbidity of the Vieux Rhone river exceeds 50 NTU. This system should consequently modify the direction and intensity of the water flow, which naturally goes from rivers toward the groundwater. For this reason, the understanding of water exchanges between the groundwater and the surface water is of major importance, as is the effectiveness of the active protection barriers formed by these infiltration basins.

The pumping site is monitored by more than 100 piezometers that are scattered throughout the site. Various hydrogeological studies have been carried out at the site scale, which highlighted the influence of groundwater pumping and Managed aquifer recharge (MAR) interventions on the aquifer levels and properties (Réfloch, 2018). At a smaller scale, a basin (5-2) located between Miribel canal and the Vieux Rhône has been the subject of more detailed studies through the implementation of a network of piezometers (Figure 1b) that provides measurements of water temperatures and piezometric levels (Réfloch, 2018). They have highlighted the following points: (a) the natural flow is to the South; (b) the infiltration basin 5-2 feeds the southern part much more than the northern part; and (c) the hydraulic barrier created below the basin disappears in a maximum of 1–2 days.

Although interesting, this work suffers from the small number of piezometers especially on the eastern part of the basin, which has prevented any detailed mapping of the hydraulic dome and its evolution over time. This is problematic in the present geological context, which exhibits sedimentary variability that generates important heterogeneity of permeability. From the surface, the vertical sedimentary sequence is composed of modern alluvial deposits composed of sands and coarse gravels of about 11–20 m of thickness. In this sequence, a main 2-m thick clayey layer has been identified in all available boreholes surrounding the basin at an average depth of 7 m. Its lateral extension, especially to the North-East where no borehole was drilled, remains unknown (Loizeau, 2013). Below this layer, inclusions of fine material were observed in boreholes with unclear organization. This modern alluvial sequence rests on a thick layer of claystones and molasse with low permeability.

### 2.2. The Seismic-Noise Experiment

The site of Crépieux-Charmy is located in a highly urbanized zone and is surrounded by several sources of anthropic seismic noise (*e.g.*, the city, highways, railway, factories). For these reasons, noninvasive hydrogeophysics and particularly seismic noise based methods were considered to be able to provide high-resolution views of the dome and its evolution over time. A preliminary study, which only involved 10 seismic sensors that recorded the ambient seismic noise over 10 days, showed strong lateral variability of the hydraulic dome (Voisin et al., 2017). In the following, we present the results of a survey using a dense seismic network that is designed to improve the monitoring resolution of the controlled changes in the groundwater flow. In all, 99 seismic nodes were deployed around the infiltration basin 5-2. They were positioned in open areas to allow good reception of the GPS satellites and synchronization of the seismic stations. The network covers a wide range of azimuths and inter-station distances (Figure 1b). The 3-C Fairfield velocimeters have a cut-off frequency of 4.5 Hz, and

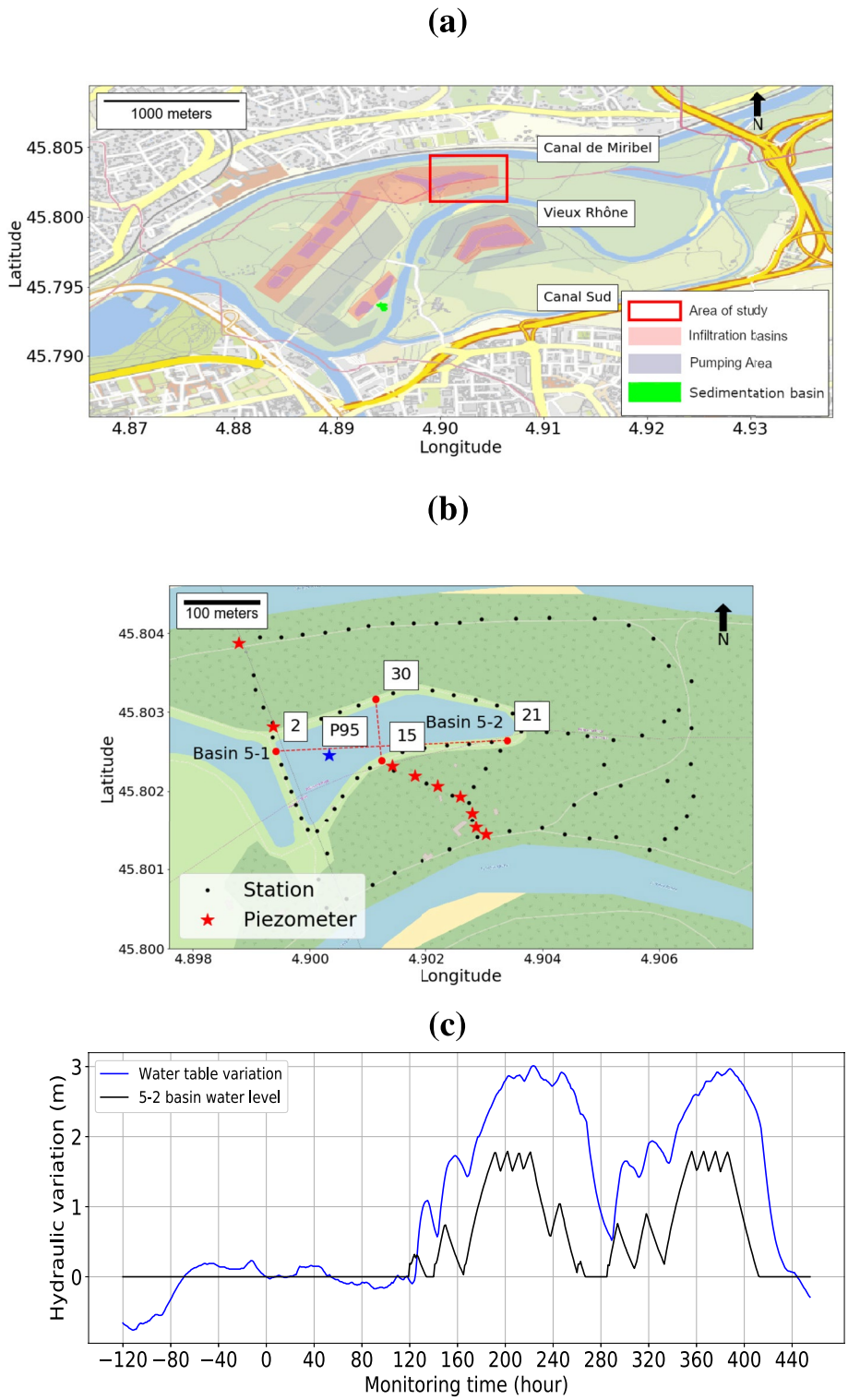



**Figure 1.** (a) Location and draft of the water pumping site of Crépieux-Charmy located to the East of the city of Lyon, in a dense urban area. It is surrounded by a railway line to the North and highways to the West, South, and East. Pumping areas, infiltration, and sedimentation basins are indicated. (b) Zoom into the studied infiltration basin 5-2, which is monitored by a network of piezometers. The seismic network is composed of 99 sensors (stations) that are deployed along paths. Stations 2, 15, 21, and 30 and piezometer P95 are used later to illustrate the main results. (c) Chronicles of the basin filling cycles with the water level measurement in the basin (black curve) and the water table variations (blue curve) measured at piezometer P95 (blue star). Time 0 marks the beginning of the seismic recordings.



19447973, 2022, 8, Downloaded from https://agupubs.onlinelibrary.wiley.com/doi/10.1029/2021WR030680 by Cochrane France, Wiley Online Library on [18/11/2022]. See the Terms and Conditions (https://onlinelibrary.wiley.com/terms-and-conditions) on Wiley Online Library for rules of use; OA articles are governed by the applicable Creative Commons License

recorded the seismic noise between 15 September and 3 October 2018 (*i.e.*, over 19 days), with a sampling frequency of 250 Hz. This represents a data volume of approximately half a terabyte.

During this period, two cycles of filling/emptying of the basin 5-2 were performed to determine the efficiency of the seismic monitoring methodology. Before the experiment, the basin was kept empty since 3 August 2018. At the beginning of the seismic experiment, the water table was measured at an elevation of 163.52 m in the piezometer P95 (well surface elevation of 169.39 m). In this condition, the unsaturated layer was 5.87 m thick at the lower point of the basin, which corresponds to a very dry state. The elevation of the dikes surrounding the basin is approximately 2.5 m above the bottom of the flat basin, with the West dike elevation culminating at 172.23 m. Figure 1c presents the evolution of the water level in the basin 5-2 and the variation of the water table measured at piezometer P95 (reference taken at time 0 hr) during the seismic monitoring period. At the beginning of the seismic acquisition, the basin 5-2 was kept empty during the first 5 days (from 0 to 119 hr) in order to acquire a base signal. The basin was then fed during 100 hr (from 120 to 220 hr). It reached the maximum level of 1.8 m at time 190 hr. The water supply was then regulated during 30 hr. The basin was then drained until emptiness in 50 hr. After a 20 hr rest period, a second filling/emptying cycle was applied in about 130 hr. Lastly, the final drainage period was monitored until the water table reached its initial level.

The basin level and the water table variations exhibited a noticeable time shift (Figure 1c), which can be observed due to the fact that the filling of the basin is not carried out in a linear way, but consists of different filling phases of various periods until. This makes it possible to analyze the phase differences between the different peaks present on the two evolution curves. During basin filling phases, the time shift corresponds to the time for water to travel through the vadose zone whose width continuously changes during the experiment. These time shifts therefore provide an estimate of the average infiltration velocity in the vadose zone. Based on a detailed analysis of the corresponding peaks of the 2 curves, we could estimate a 0.3 m/hr infiltration velocity during the first infilling whereas it rises to 0.5 m/hr during the second infilling. This observation is consistent with an increase in average water content between the two cycles: before the first infilling, the vadose zone was at residual saturation when the water content was much higher at the beginning of the second infilling which probably followed an incomplete drainage. The observed difference could then be attributed to an increase of the medium relative permeability and to a progressive capillary wetting during the first infiltration event.

## 3. Seismic-Noise Data Processing and Analysis

To compute reliable tomographic maps of the velocity variations, the workflow includes several steps, as sketched in Figure 2. In this section, we focus on the steps that start after the data recording and until the velocity variations are obtained per pair of stations. The first stage is the pre-processing, which simply consists of formatting and sorting the data set. A beamforming analysis is performed on these raw data, to assess the spatial origin and time stability of the seismic sources (Section 3.1).

The second step encompasses various signal-processing steps that were chosen for calculation of the cross-correlations per sensor and component pair (Section 3.2). By re-sorting these cross-correlations as a function of receiver distance, the propagation of the wavefield can be represented and analyzed for each component (Section 3.3). This step provides a clear separation of the seismic wavefield between the ballistic and coda parts that will be crucial for the third step, the relative seismic velocity $\delta v/v$ computations (Section 3.4). The final data set is composed of 4,851 hourly $\delta v/v$ measurements, which will be the input to get hourly tomographic inverse maps, as discussed in Section 4.

### 3.1. Source Analysis Using a Beamforming Approach

The beamforming compares the seismic wavefield with waves propagating under different azimuths and velocities (or slownesses). Beamforming has been used in many seismic-noise studies; for example, for phase velocity estimations (Harmon et al., 2008), source directionality assessment (Behr et al., 2013), and surface-wave tomography (Roux & Ben-Zion, 2017; Wang et al., 2020). The use of dense and large arrays with a wide azimuthal cover ensures accurate resolution (Rost & Thomas, 2002). The computation relies on the plane-wave assumption so that sources located within the receiver array or any kind of arrivals that are not recorded by several receivers will not be emphasized. The processing uses the differences in arrival with the center of the array as a reference



19447973, 2022, 8, Downloaded from https://agupubs.onlinelibrary.wiley.com/doi/10.1029/2021WR030680 by Cochrane France, Wiley Online Library on [18/11/2022]. See the Terms and Conditions (https://onlinelibrary.wiley.com/terms-and-conditions) on Wiley Online Library for rules of use; OA articles are governed by the applicable Creative Commons License

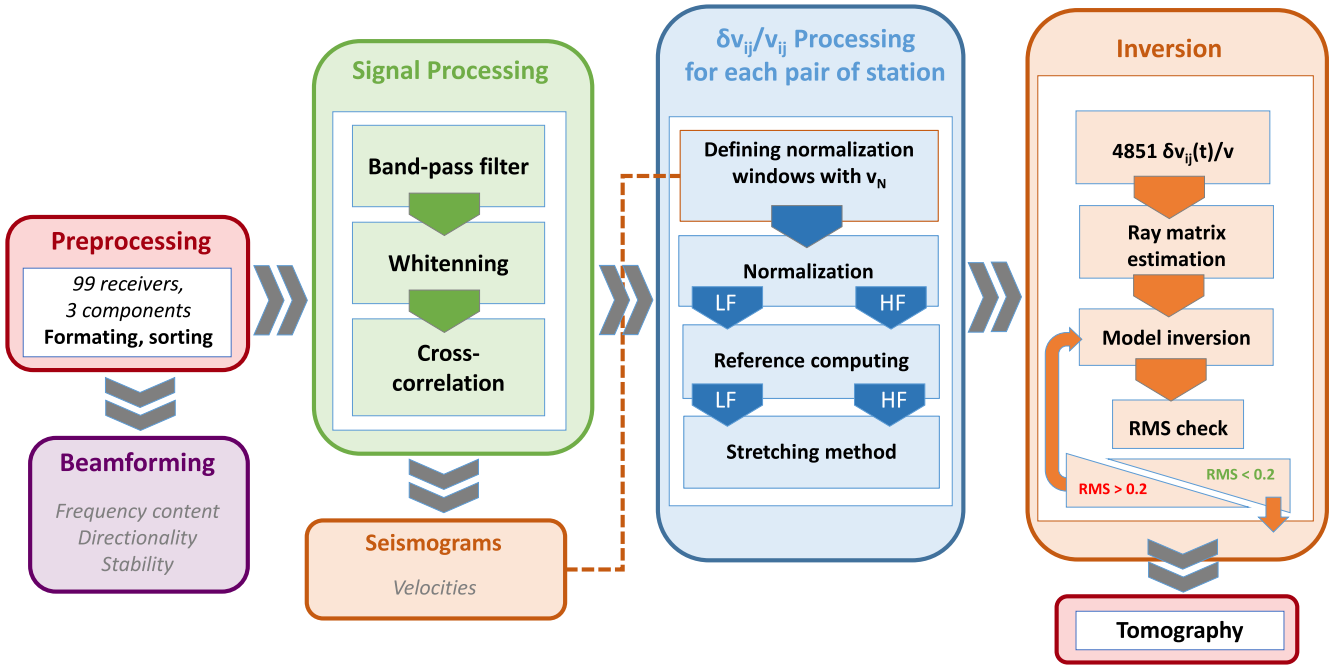



**Figure 2.** Seismic-noise data processing workflow designed to compute the dynamic two-dimensional tomographic maps of the seismic velocity variations. The beamforming stage offers access to the spatial distribution of the seismic noise sources and its stability. The three-component seismograms provide understanding of the seismic wavefield and identification of the different seismic phases. The $\delta v/v$ processing can be performed in the low or high frequency range according to the cross-correlation spectral properties.

(Boué et al., 2013), and it can be performed in different frequency ranges and for different components. This analysis is particularly important here as our survey is performed in a highly urbanized zone (Figure 1a), where the origin of the seismic noise can vary both in space and time due to the presence of multiple time-varying sources (*e.g.*, highways, railways, factories).

A typical example of the beamforming outputs separately computed for the two horizontal components and then gathered after summation is shown in Figure 3. This was computed in the (2–5 Hz) frequency range using 24-hr time windows with a code adapted from the double beamforming algorithm of Boué et al. (2013). The beamforming outputs appear stable over time and show almost isotropic patterns at 400 m/s velocity, with a slight East-West dominance. Figure 3d highlights the variability of the amplitude power over the monitoring time. It is computed over 1-hr time windows, while the black dashed line represents the amplitude smoothed over a 24-hr moving window. The quieter periods appear during weekends (gray area). We will see in the following that these noise conditions appear to be sufficiently stable and isotropic at the site to produce consistent and stable wavefields over most sensor pairs. We note that during weekdays (*i.e.*, 48–72 hr, 120–144 hr), the maximal energy comes from the West, where there is the northern ring road of the Lyon metropolis.

### 3.2. Cross-Correlation Computations

For the horizontal components, the $ij$ ray has an azimuth $\theta = \widehat{ijN}$ (with the North) corresponding to the path between the two receivers, which will very rarely match the recording North-South ($S_{i,N}$) and East-West components ($S_{i,E}$). As suggested by Roux (2009), the equivalent radial ($S_{i,R}$) and transverse ($S_{i,T}$) components measured by the receiver $R_i$ along the $ij$ ray can be recovered using the relations:

$$S_{i,T} = S_{i,N}\sin\theta + S_{i,E}\cos\theta \text{ and } S_{i,R} = S_{i,N}\cos\theta + S_{i,E}\sin\theta. \quad (1)$$

The cross-correlation of seismic noise signals recorded by two receivers ($R_i$, $R_j$) is theoretically an estimate of the Green's function, that is, the impulse response of the Earth between these two receivers, if the noise sources are isotropically distributed around them. The product of the cross-correlation in the three projected dimensions ($R$, $T$, $Z$) of the receivers pair ($R_i$, $R_j$) is a tensor of nine components that represents the Green's function in space:



19447973, 2022, 8, Downloaded from https://agupubs.onlinelibrary.wiley.com/doi/10.1029/2021WR030680 by Cochrane France, Wiley Online Library on [18/11/2022]. See the Terms and Conditions (https://onlinelibrary.wiley.com/terms-and-conditions) on Wiley Online Library for rules of use; OA articles are governed by the applicable Creative Commons License

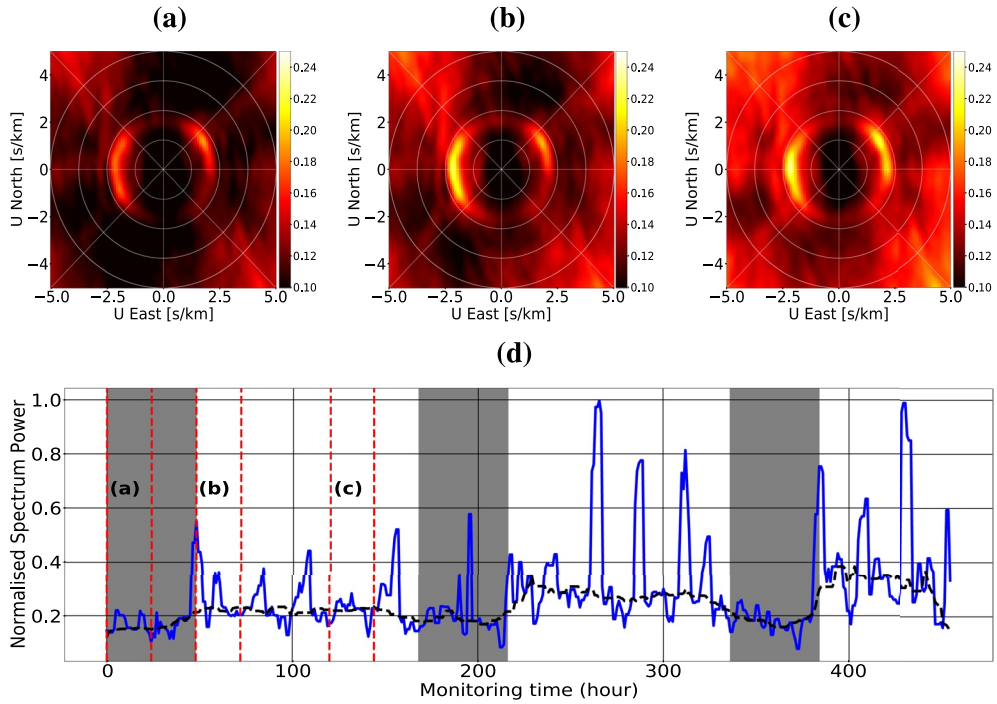



**Figure 3.** Horizontal beamforming amplitudes averaged over 24-hr time windows in the dominant (2–5 Hz) frequency range for three monitoring periods: (a) 0–24 hr (b) 48–72 hr (c) 120–144 hr. The *x*-axis represents the slowness from the East and the *y*-axis represents the slowness from the North, which can be recovered for all directions with white circles. (d) Evolution of the spectral energy over the monitoring time (blue curve) with the smoothed variation over 24 hr (dashed line) averaged in the (2–5) Hz band. Gray zones correspond to weekend periods.

$$\mathbf{G}(i,j) = \begin{pmatrix} TT & TR & TZ \\ RT & RR & RZ \\ ZT & ZR & ZZ \end{pmatrix} \tag{2}$$

When dealing with the same components, we obtain the *TT* (transverse-transverse), *RR* (radial-radial), and *ZZ* (vertical-vertical) coefficients that compose the diagonal of the **G** tensor. All of the other coefficients in $\mathbf{G}(i,j)$ obtained by correlating different components of the signals (for instance *R* and *Z*) are not addressed in this paper.

For all of the components, to eliminate spurious energetic events and to balance the spectral content (Shapiro et al., 2005), the signals are first whitened on a daily basis between 1 and 20 Hz, which is the band of interest at our scale. The processed signals are then sliced in $T_w = 1$ min long time windows, and normalized by the energy of each time slice to get diagonal coefficients of the $\mathbf{G}(i,j)$ tensor:

$$G(i,j)_{KK} = \frac{S_{i,K}(t) \otimes S_{j,K}(-t)}{\sqrt{\int_0^{T_w} S_{i,K}^2(\tau)\,d\tau \int_0^{T_w} S_{j,K}^2(\tau)\,d\tau}} \text{with } K = T, R \text{or } Z \tag{3}$$

Eventually, these cross-correlations are stacked over 10 mn or 1 hour, to improve the signal-to-noise ratio without degrading the dynamics of the variations that we want to reconstruct. An illustration of the *TT*, *RR*, and *ZZ* final correlograms is shown in the [−2.8, 2.8] s time lag window in Figure 4 for the 324 m spaced ($R_2$, $R_{21}$) pair of receivers. The red trace represents the overall averaged cross-correlations for this pair, and will be a reference when computing the velocity changes $\delta v/v$ in Section 3.4. The *TT* correlograms obtained for this pair of stations that are mainly oriented East-West show acceptable symmetry. They show a dominant wave packet that arrives at ±0.9 s and corresponds to an apparent velocity of 360 m/s. Contrary to the *TT* component, the *RR* and *ZZ* components show more disturbances, which is possibly related to the local noise generated by the pumps. They are also



19447973, 2022, 8, Downloaded from https://agupubs.onlinelibrary.wiley.com/doi/10.1029/2021WR030680 by Cochrane France, Wiley Online Library on [18/11/2022]. See the Terms and Conditions (https://onlinelibrary.wiley.com/terms-and-conditions) on Wiley Online Library for rules of use; OA articles are governed by the applicable Creative Commons License

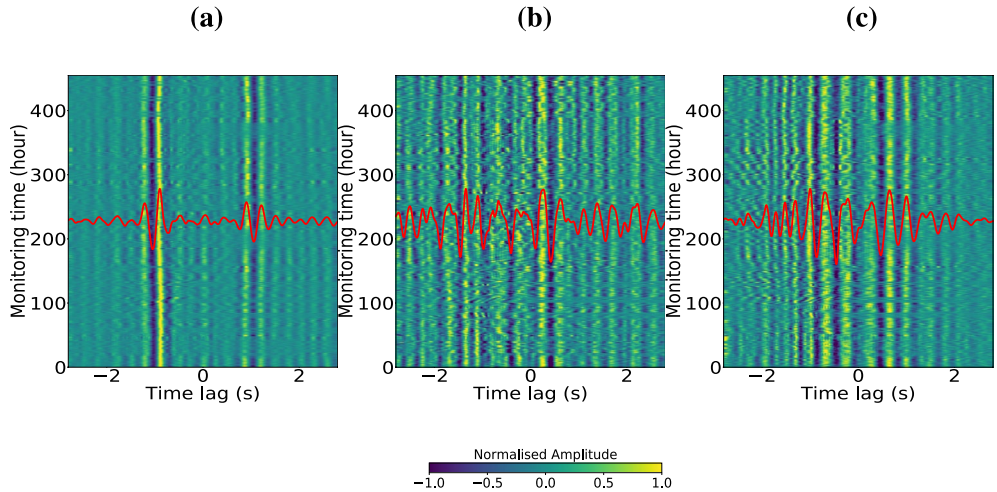



**Figure 4.** (a) *TT*, (b) *RR*, and (c) *ZZ* correlograms computed between 2 and 5 Hz for each component of the 324 m spaced ($R_2$, $R_{21}$) pair of receivers, over the 19 recording days. Time of monitoring is going upward. Red curve is the overall averaged cross-correlations for the component.

more complex, with many different events arriving at several times. In the following, we address the complexity of the seismic wavefield using all available distances, through the network of 99 sensors.

### 3.3. Analysis of the Seismograms

To analyze the multi-component wavefields which will be used for monitoring purposes, we gathered all averaged cross-correlations filtered in the (2–5 Hz) frequency band, taking into account all station pairs available through the deployment of the 99 sensors, which provides 4,851 traces with distances ranging from 12 to 645 m (Figure 5), with few with distances beyond 550 m.

These figures show relatively well separated ballistic waves with different patterns according to the component. They are all symmetric, which reinforces the hypothesis of the isotropic spatial distribution of seismic sources. The *TT* component is dominated by a surface wave with an apparent velocity slightly over 400 m/s, while the *RR* component shows a dominant wave that propagates slightly faster. The *ZZ* component is more complex, with various waves of similar amplitudes but with a wide range of velocities, from 1850 m/s for the first arrivals to 200 m/s for the slowest, which is consistent with previous observations made by Garambois et al. (2019). It should be noted that the available energy is stable as a function of distance and is relatively limited in frequency, with a peak between 2 and 4 Hz, and a rapid decline thereafter, with almost no energy beyond 10 Hz. A more

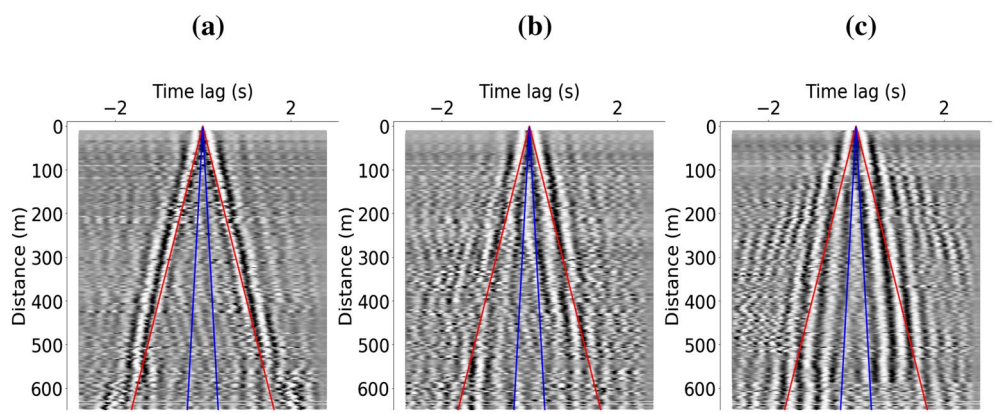



**Figure 5.** Seismograms of the (a) *TT*, (b) *RR*, and (c) *ZZ* components, obtained after stacking all of the cross-correlations computed for the whole experiment and all possible inter-station distances. Red and blue lines highlight the velocities of 400 and 1,850 m/s respectively.



19447973, 2022, 8, Downloaded from https://agupubs.onlinelibrary.wiley.com/doi/10.1029/2021WR030680 by Cochrane France, Wiley Online Library on [18/11/2022]. See the Terms and Conditions (https://onlinelibrary.wiley.com/terms-and-conditions) on Wiley Online Library for rules of use; OA articles are governed by the applicable Creative Commons License

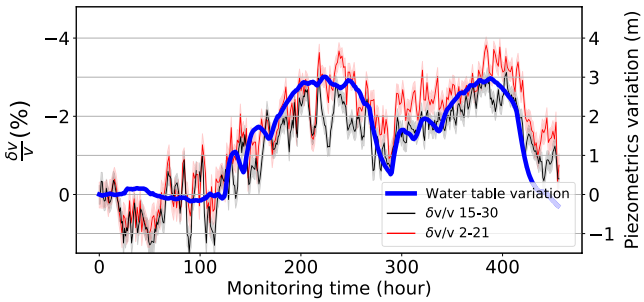



**Figure 6.** Evolution of the piezometric level (solid blue) measured at piezometer P95 and of the hourly $\delta v/v$ velocity variations computed between the station pairs $R_2$-$R_{21}$ (in red, East-West oriented) and $R_{15}$-$R_{30}$ (in black, North-South oriented) over the entire duration of the experiment, between 2 and 5 Hz. Shadow areas represent the uncertainty on the measurement, obtained considering the maximum stretching function $\epsilon_{max} \pm \sigma$ ($\sigma$ being the variance).

detailed analysis of the wavefield through phase velocity dispersion analysis of the 3C data is provided in Text S1 in Supporting Information S1.

### 3.4. Computations of Velocity Variations

The *TT* seismogram shows a satisfactory signal-to-noise ratio (Figure 5a) and a relatively simple symmetric wavefield dominated by the fundamental mode of Love waves between 2 and 9 Hz (Figure S1 in Supporting Information S1). In addition, as shown in Section 3.1, the horizontal components of the noise are relatively stable over time and azimuth. For these reasons, the velocity variations have been computed considering the ballistic Love waves, which dominate the *TT* data. This analysis is performed with the stretching technique (Sens-Schönfelder & Wegler, 2006), which consists in quantifying the similarity of each hourly cross-correlation, stretched by a set of $\epsilon$ values, with the overall mean of the cross-correlation signal that is considered as a reference. The quantification is made by cross-correlating the two signals in the time window of the dominant ballistic wave, that is, the Love wave. This linear search automatically extracts the maximum correlation coefficient and the corresponding stretching factor $\epsilon_{max}$. This automatic analysis is controlled by a rejection process based on the value of the correlation coefficient: values below a coefficient of 0.8 are ignored, which represents 26.7% rejection. The computations provide the optimized time shift of the signal $dt$ at a time $t$ compared to the reference, and consequently the relative velocity variations for each trace of the correlogram $\delta v/v = -dt/t = \epsilon_{max}$.

The process was applied to the 4,851 available correlograms in the (2–5) Hz frequency band and provided hourly $\delta v/v$ estimates relative to a reference during the whole acquisition for all 4,851 pairs. In the following, we shifted the relative $\delta v/v$ values to ensure that $\delta v/v = 0$ at $t = 0$ s, the starting time of the seismic experiment, for all pairs.

The result of this cross-correlation processing is a set of 4,851 cross-correlation functions. They are supposed to be the Green's function between two stations along a path. Each of them indeed carries information about the global changes between the two stations and it is worth visualizing these $\delta v/v$ variations, even if the spacial resolution is not optimized at this point. In Figure 6, the $\delta v/v$ variations for the $R_2 - R_{21}$ and $R_{15} - R_{30}$ pairs are compared to the relative water table variations measured at the P95 piezometer. The direct paths of these two pairs both cross the basin with different azimuths (see Figure 1). The $\delta v/v$ and water table curves are anti-correlated: negative velocity variations are associated with rising water table. This anti-correlation has often been observed when velocity variations are estimated on surface waves (Voisin et al., 2016, 2017) and quantitatively well explained using a poroelastic fluid substitution approach (Garambois et al., 2019). The hourly $\delta v/v$ measurements show high frequency variations, that we interpret as measurements uncertainties linked to fluctuating hourly reconstructed waveforms with different signal-to-noise ratio. In addition, we note that the two filling cycles show some small discrepancies highlighting some delays and nonlinear responses, especially when considering (a) the small $\delta v/v$ variations observed before the filling; (b) the different $\delta v/v$ responses depending on the pair of stations between the two maxima, and (c) the failure for $\delta v/v$ to return to the initial state at the end of the experiment. These discrepancies might come from two reasons. First, the major difference between the two measurements is that the piezometer measurement provides only local information, while the $\delta v/v$ integrates information along the path between two stations. Second, the potential sensitivity of $\delta v/v$ measurements to water saturation changes within the unsaturated zone can affect the consistency. In order to prevent any ambiguous interpretation, we aim at implementing a tomography process with very high spatial resolution that will lead us to a discussion on the effect of the unsaturated zone.

### 3.5. Frequency/Depth Analyses

Velocity variations shown in Figure 6 were computed after selecting the (2–5 Hz) frequency band dominating cross-correlated signals. We additionally show in Figure S2a in Supporting Information S1 the $\delta v/v$ evolution over time as a function of frequency for the $R_2 - R_{21}$ pair. This frequency analysis confirms that velocity variations related to hydrological cycles are observed only in a very limited frequency band, with a lack of sensitivity both below 2 Hz but also above 5.5 Hz. The kernel sensitivity computations performed for Love waves (Figure S2b in



19447973, 2022, 8, Downloaded from https://agupubs.onlinelibrary.wiley.com/doi/10.1029/2021WR030680 by Cochrane France, Wiley Online Library on [18/11/2022]. See the Terms and Conditions (https://onlinelibrary.wiley.com/terms-and-conditions) on Wiley Online Library for rules of use; OA articles are governed by the applicable Creative Commons License

19447973, 2022, 8, Downloaded from https://agupubs.onlinelibrary.wiley.com/doi/10.1029/2021WR030680 by Cochrane France, Wiley Online Library on [18/11/2022]. See the Terms and Conditions (https://onlinelibrary.wiley.com/terms-and-conditions) on Wiley Online Library for rules of use; OA articles are governed by the applicable Creative Commons License

Supporting Information S1) support these observations: the sensitivity of Love waves to changes in the environment is maximum between 2 and 7 m depth and is only significant and constant for frequencies between 2 and 5 Hz. In contrast, lower and higher frequencies show larger sensitivity kernels at depths larger than the lowest position of the water table. These computations seem to confirm the observation that the velocity variations captured from the cross-correlations when computed in the (2–5 Hz) frequency range are the most sensitive to the fluctuations of the water table and water content occurring within the modern and coarse alluvial deposits located between 2 and 7 m depth.

## 4. High-Resolution Tomography Monitoring

From these integrated $\delta v/v$ measurements, we aim to produce high resolution time-lapse spatial $\delta v/v$ maps to emphasize the shape of the water dome and the potential water fluxes.

### 4.1. The Tomographic Scheme

For this purpose, we use a tomographic approach by inverting all of the paths in the 2–5 Hz frequency range with a 1-hr time step. A similar approach was first proposed by Brenguier et al. (2008) for volcanic applications, and then taken further by Clements and Denolle (2018) at a larger scale, to regionalize the $\delta v/v$ measurements obtained on the coda waves for groundwater applications. Here, we use the (straight) ray theory approach of Barmin et al. (2001), to carry out fast and reliable tomography, as further adapted by Mordret et al. (2014) to obtain group velocity maps from ballistic-wave seismic-noise analysis. This optimization process requires the use of a regularization function (here, as a spatial Gaussian smoothing term) and an additional term that constrains the amplitude of the perturbations according to the local path density.

The inversion scheme follows an iterative process: at each iteration, the rays with the largest root mean square (RMS) error (>70%) are discarded for the following iteration. These large errors might be related to bad signal-to-noise ratios in the cross-correlation computation due to local sources or artefacts in the $\delta v/v$ measurements. To maintain acceptable spatial resolution (a model obtained with at least 40% of the initial number of rays), the inversion is stopped after three iterations. The velocity variations are mapped onto a $44 \times 22$ roughly rectangular grid with square mesh (19.9 m). The spatial Gaussian term is characterized by a correlation length of 50 m and a smoothing strength of 0.05. These parameters were selected as a satisfactory compromise between resolution and stability of results, after different attempts, including checkerboard tests. The detailed results derived at 210 hr of monitoring are shown in Figure 7. This shows in (a) the map of the $\delta v/v$ relative to the beginning of the experiment (time 0).

At the beginning of the tomography process, the data set contains 4,010 rays that are homogeneously distributed in azimuth and distance (Figure 7b). At the end of the third iteration, 2,705 rays are retained, as shown in Figure 7c. We note that no particular azimuth is removed by the RMS checking process, despite the polarization of the sources discussed in Section 3.1. Conversely, short offset rays that are favorable to mixed arrivals (interference) clearly tend to be eliminated. The RMS error appears to be homogeneous on the whole grid (Figure 7d) and lower than 0.15, except for a few very sparse grid points that show larger errors. At the final iteration, that is, after removal of the raypaths with large RMS, the ray density remains high. Indeed, some cells are illuminated by more than 150 rays, while on average, there is a density of 90 rays per cell, except at the edges of the grid (Figure 7d). It needs to be noted that additional tests carried out with the help of checkerboard tests have confirmed the great resolution of the tomography with this illumination.

The $\delta v/v$ map of Figure 7a shows a maximum of the velocity variations in the southern sector of the infiltration basin, slightly East of the filling point. We also see fairly moderate values within the basin, as well as a North-South variation. The eastern part of the exploration area remains relatively static, with almost no velocity change.

10.1029/2021WR030680

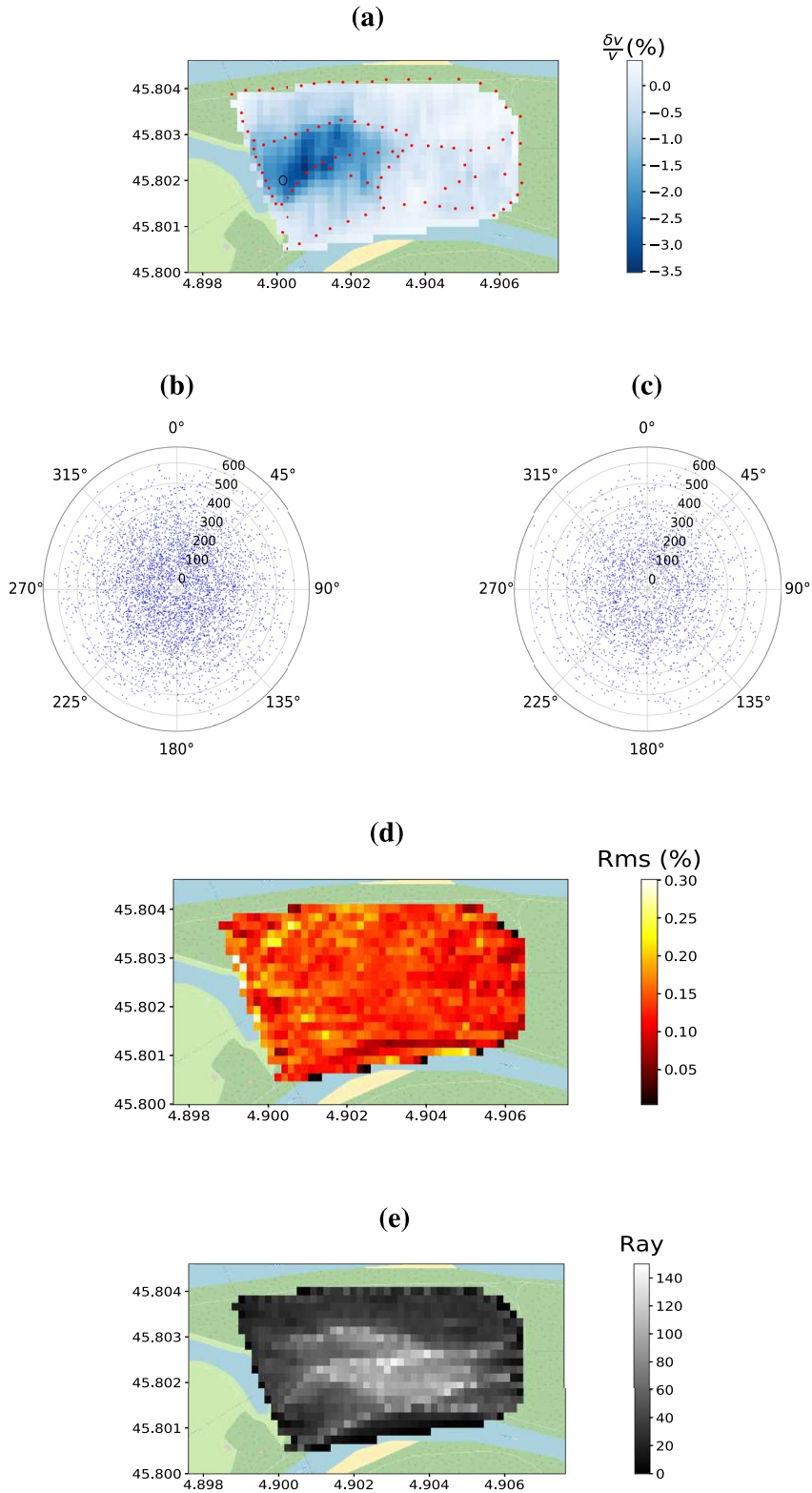



**Figure 7.** Results of the inversion process illustrated at 210 hr of monitoring. (a) $\delta v/v$ map relative to the start of the experiment, as obtained after three iterations of the inversion process. The black circles localize the filling point. (b) Initial and (c) final distributions of the rays in terms of the azimuth and distance. (d) Root mean square error map. (e) Number of raypaths per cell.



19447973, 2022, 8, Downloaded from https://agupubs.onlinelibrary.wiley.com/doi/10.1029/2021WR030680 by Cochrane France, Wiley Online Library on [18/11/2022]. See the Terms and Conditions (https://onlinelibrary.wiley.com/terms-and-conditions) on Wiley Online Library for rules of use; OA articles are governed by the applicable Creative Commons License

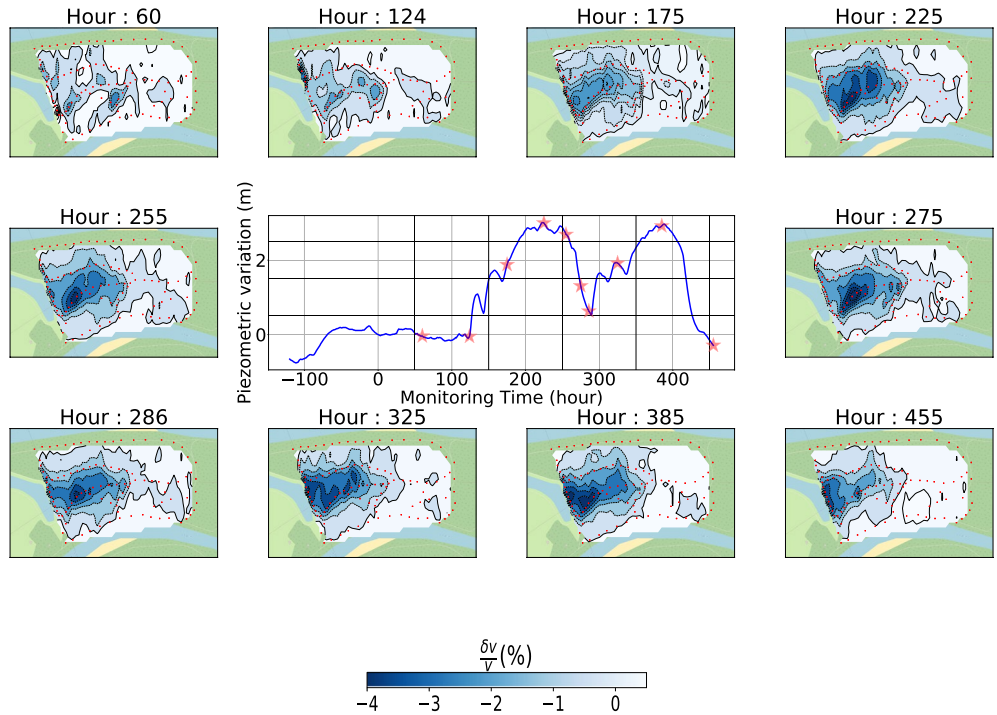



**Figure 8.** Evolution of the $\delta v/v$ maps for 10 different key moments of the controlled monitoring experiments. The central graph shows the relative evolution of the water table measured at piezometer P95. The red stars highlight the moments for which the maps are shown.

### 4.2. Evolution of the Velocity Variation Tomographic Maps

A similar inversion procedure is carried out for each hour of the monitoring experiment, with a RMS error between 9.2% and 18.8%, where the number of rays varies from 1940 to 4851. This allows us to obtain a dynamic animation of the spatial variations in the relative velocity. It must be noted that a movie showing the 3D evolution of the hourly velocity variation tomographies is available in Movie S3. In Figure 8, we isolated the maps obtained at 10 characteristic key moments. To facilitate their reading, the center of Figure 8 shows the continuous variations of the water table level measured at piezometer P95 (*i.e.*, near the point of injection), as well as the key moments (red stars). It should be noted that the piezometer data provide information on the variations of the water table but not on the infiltration in the unsaturated zone, which probably started a few hours before.

During the first 60 hr, we observe an initial state showing little localized negative velocity variations, possibly related to natural transfers with rivers, or residual saturation in the vadose zone from past infiltration or precipitation events. The infilling of the basin starts at 119 hr, and the maps highlight the build-up of a negative $\delta v/v$ already established at 124 hr which culminates at 225 hr, in agreement with measured water table variations. At this time, well-localized patches are visible within the basin, which form what looks like a dome that stretches in the direction of the basin. Outside the basin, smaller negative velocity variations can also be seen. We note that $\delta v/v$ slightly decreases in value during the drainage cycle, and then increases again during the second filling cycle, only to decrease again during the second drainage. Surprisingly, although decreasing, the system does not return to equilibrium at the end of the experiment (at 455 hr), unlike the piezometric measurements. This appears to indicate that water exchanges are still ongoing in the vadose zone with a clear effect on the velocity of surface waves. This point will be discussed afterward.

## 5. Discussion

In the previous sections, we showed that passive seismic interferometry used with a dense network can provide time-lapse information of hydrological variations with very high spatial and temporal resolution. Indeed, the dynamics of velocity changes and of the piezometric variations recorded locally appear relatively well correlated



19447973, 2022, 8, Downloaded from https://agupubs.onlinelibrary.wiley.com/doi/10.1029/2021WR030680 by Cochrane France, Wiley Online Library on [18/11/2022]. See the Terms and Conditions (https://onlinelibrary.wiley.com/terms-and-conditions) on Wiley Online Library for rules of use; OA articles are governed by the applicable Creative Commons License

19447973, 2022, 8, Downloaded from https://agupubs.onlinelibrary.wiley.com/doi/10.1029/2021WR030680 by Cochrane France, Wiley Online Library on [18/11/2022]. See the Terms and Conditions (https://onlinelibrary.wiley.com/terms-and-conditions) on Wiley Online Library for rules of use; OA articles are governed by the applicable Creative Commons License

at first glance. This new view allows a detailed study of this relationship. In particular the quantitative approach derived with a limited number of sensors and a single filling cycle by Voisin et al. (2017) and Garambois et al. (2019) can be further discussed. Their analysis seemed to show a linear relationship in which 1% of $\delta v/v$ measured on surface waves roughly corresponds to 1 m of water table variations. In this section, we will discuss further the hydrological impacts of our seismological results according to three points: (a) the contribution of a 3D representation of the water dome and flows with a very high resolution compared to water table local measurements; (b) the differences between $\delta v/v$ and piezometer data, which highlights the additional sensitivity of seismic data to water content changes occurring in the unsaturated zone; and (c) the applicability of such seismic monitoring for operational but also for other hydrological monitoring purposes.

### 5.1. Contribution of the Seismic Monitoring for 3D Characterization of the Hydraulic Barrier

The groundwater variations observed during the infiltration cycles on this site were previously derived from precise temperature and water table data measured from a sparse number of piezometers (Réfloch, 2018). They could nonetheless put some constraints on the preferential flow of the system; namely: (a) the natural North-South flow direction of the water table is reversed; (b) the hydraulic dome has a very steep slope; and (c) the hydraulic dome created by the basin is not symmetric, with the groundwater response stronger and faster for the southern part of the site.

To better show the geometry of the seismic signature generated by the two filling cycles, the velocity variations have been plotted at the times corresponding to the two absolute peaks relative to the establishment of the hydraulic dome (Figure 9). Additionally, we computed the horizontal gradients observed at the same two periods (Figure 9), where the amplitudes and directions are represented by arrows. This representation highlights the significant fluxes observed from the middle of the infiltration basin to the outside. What stands out from Figure 9 is the elongation of the dome along the stretch of the basin. This also highlights the steepness of the dome at the two maximums, with a much steeper slope on the South side. This is possibly due to the concave shape of the basin that promotes converging flows and/or to accumulation of water in the dyke. The maximum velocity decrease is thus located at the South edge of the basin nearby the basin dyke where no piezometer is available. The West-East spatial variability is also very high, with a strong drop in the areas outside of the basin. This is even more true after the drainage of the second cycle, where almost no variation is visible on the eastern side: the basins only provide hyper-localized protection. On the Western part, these 3D plots show a strong velocity gradient, in the dyke separating basin 5-2 from the emptied adjacent western infiltration basin 5-1 (Figure 1). Despite located on the edge of the tomography, this sharp variation is well constrained by the large number of rays illuminating this area (Figure 7). The dyke is composed of finer compacted material and is likely to better retain water due to a lower permeability. It must be noted that the velocity decrease is stronger during the second filling cycle. The second imbibition in the dyke probably benefited from the first wetting phase.

All of these high-resolution quantitative images will undoubtedly be crucial input to better constrain numerical models designed to analyze the impact of the infiltration basin on river/aquifer exchanges.

### 5.2. Comparison Between Seismic and Piezometric Time Evolution: Role of the Unsaturated Zone

The high-resolution dynamic maps allows us to compare the computed seismic velocity variations with available hydrological data, both in time and space. Figure 10a presents piezometers P95 and S20 locations used for the temporal comparison while piezometers located along a generally North-West South-East transect are used for the space analysis. The $\delta v/v$ data were extracted from dynamic tomographies at cells located near piezometers of interest.

The temporal evolution of $\delta v/v$ and water table levels are plotted in Figures 10b and 10c. The hourly $\delta v/v$ data are smoothed over 10 hr to attenuate high frequency variations and they generally follow the water level variations for the two selected areas. At the beginning of the experiment, the comparison shows the instability of the seismic monitoring approach when the water-table variations are small. During the first infilling, both signals follow a similar increasing trend and reach a maximum at the same time. The decrease during the drainage phases is more significant for the water table level than for the seismic measurement. A similar trend is observed during the second infilling. Both signals reach their maximum at the same time and with the same intensity as for the first infilling. To better illustrate these behaviors, it is convenient to represent H-plots, displaying the water table

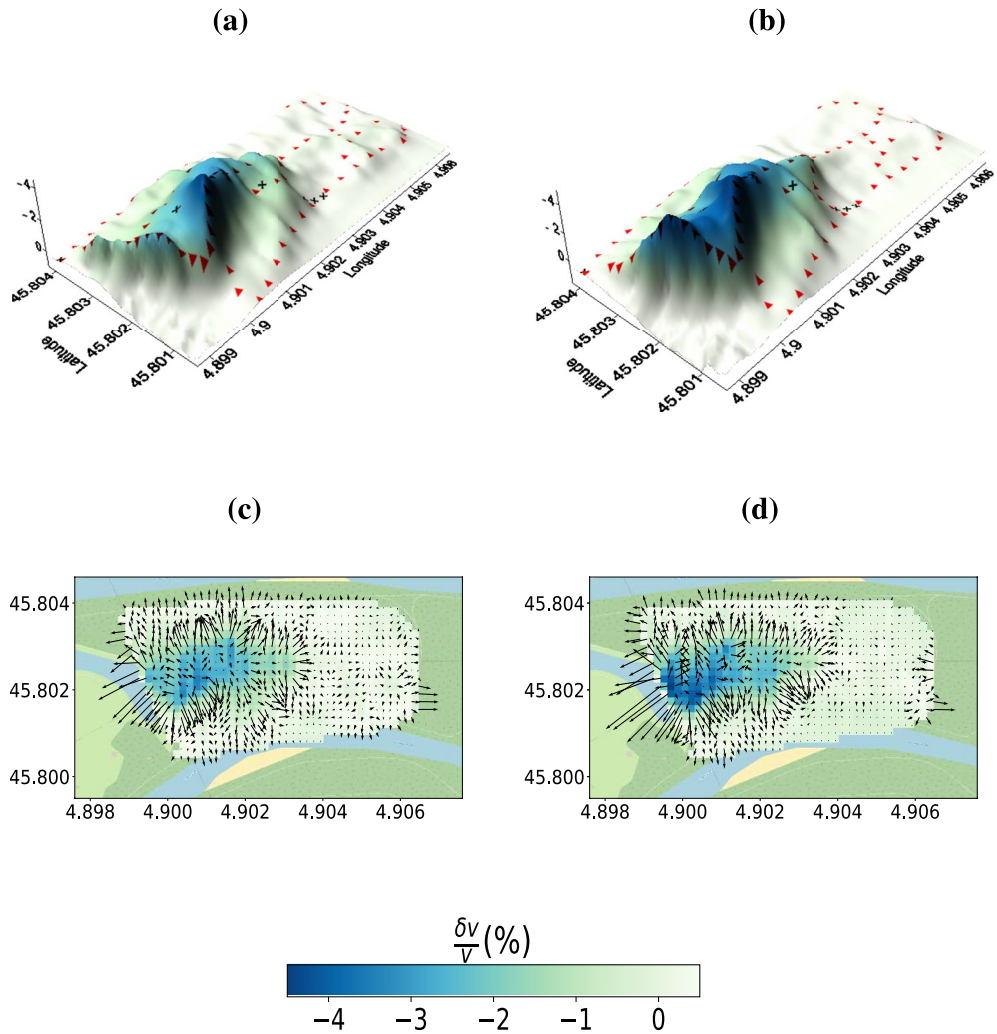



**Figure 9.** Three-dimensional views of the seismic velocity variations observed at the maximum of each infiltration cycle; that is, at (a) 225 hr and (b) 390 hr. The red triangles represent the seismic sensors, and the black crosses indicate the piezometers. The corresponding horizontal gradient maps are also shown for (c) 225 hr and (d) 390 hr.

level as a function of $\delta v/v$ in Figure 10d (for S20) and Figure 10e (for P95). During the initial infilling (blue dots), the proportionality relationship between the changes in the velocity and the water table variations roughly fits that proposed by Voisin et al. (2017): 1% = 1 m, which is marked by the dashed line. During this phase, the increase of the saturated level is the main contribution to velocity variations, as numerically shown by Garambois et al. (2019) who considered a sharp delineation between the saturated zone and the dry soil. When the basin has been emptied, the drainage phase (red dots) starts with a very clear and quick drop of the water table level, contrary to velocity variations which decrease much slower and remain far from reaching the initial state, as already noticed on the tomography maps (Figure 8). Similar trends are observed during the second infilling (green dots) and drainage (orange dots). During the last drainage, the velocity variations decrease is much slower than the water table with −1% still remaining after 3 days.

Both Figures 10d and 10e present a well-identified hysteretic behavior where the first infilling (blue dots) and the final drainage (orange dots) clearly follow two different paths. This behavior is observed for both the piezometer P95 located inside the basin and the piezometer S20 located close to the dyke outside the basin. The first drainage (red dots) and second infilling (green dots) describe a secondary loop nested in the main one for the piezometer S20. This effect may be linked with the imbibition/drainage within the dyke. During the last drainage, the moment when the level of the water table crosses zero again, around 440 hr, the variations in velocity are still of the order of 2%. Using a poroelastic approach (Garambois et al., 2019), one can compute the expected velocity



19447973, 2022, 8, Downloaded from https://agupubs.onlinelibrary.wiley.com/doi/10.1029/2021WR030680 by Cochrane France, Wiley Online Library on [18/11/2022]. See the Terms and Conditions (https://onlinelibrary.wiley.com/terms-and-conditions) on Wiley Online Library for rules of use; OA articles are governed by the applicable Creative Commons License

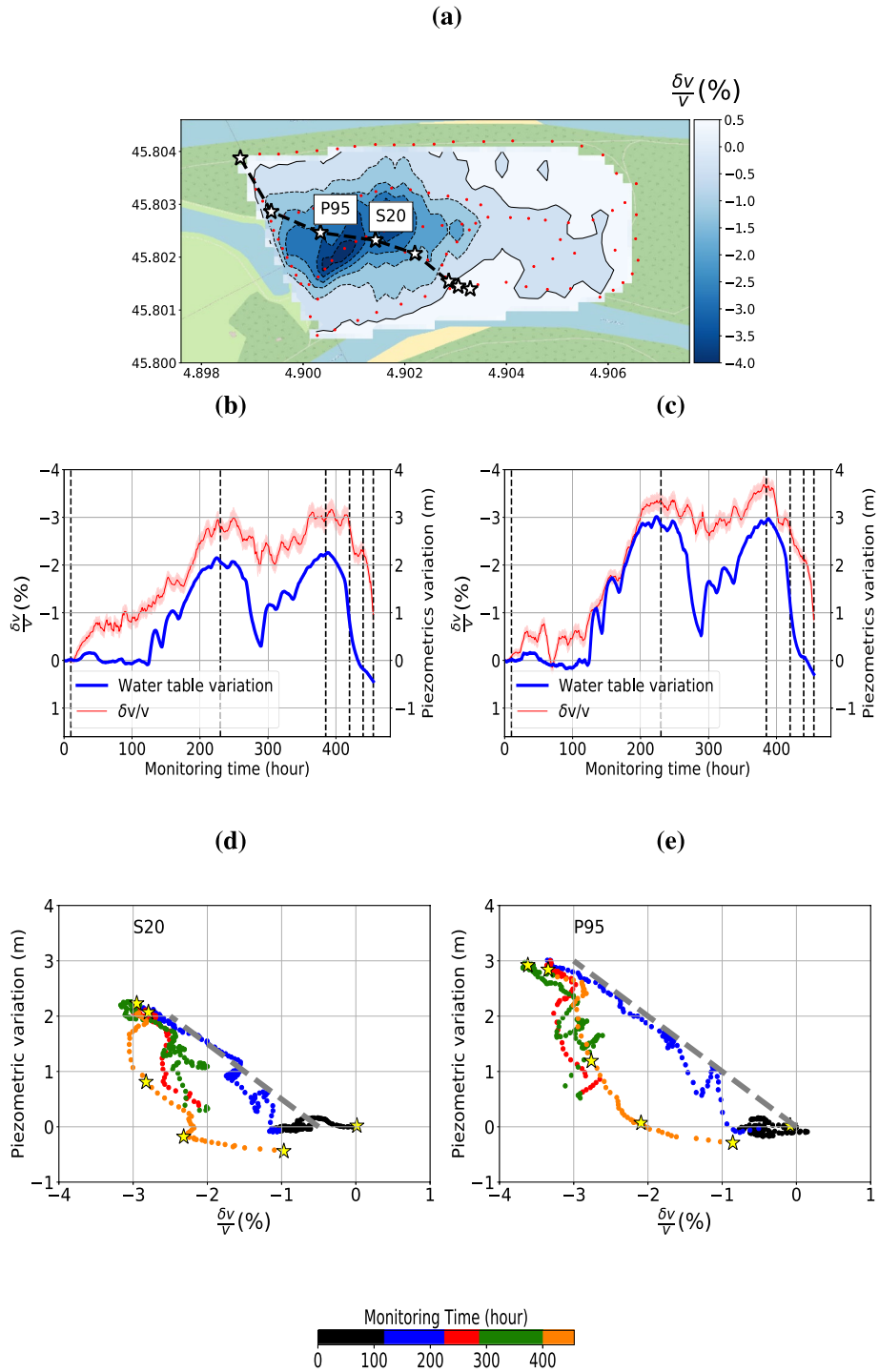



**Figure 10.** Dynamics of $\delta v/v$ values extracted from the tomography approach from selected cells. (a) Superimposition of the $\delta v/v$ tomography obtained at 225 hr, around the peak of the first filling cycle and a transect of piezometers, denoted by stars. Comparison between $\delta v/v$ measurements (red curves) smoothed on a 10 hr time window and averaged on the cells surrounding piezometers (b) S20 and (c) P95 and the corresponding water table variations (blue curves). Water table versus $\delta v/v$ evolution for the (d) S20 and (e) P95 areas. A time stamp is indicated through the color of the dots (empty basin: black; first infilling: blue; first drainage: red; second infilling: green; final drainage: orange). The gray dashed lines highlight the 1m-1% linear relationship. The vertical dashed lines of panels (b and c) which are highlighted by stars in panels (d and e), mark the 6 selected times studied in Figure 11.



19447973, 2022, 8, Downloaded from https://agupubs.onlinelibrary.wiley.com/doi/10.1029/2021WR030680 by Cochrane France, Wiley Online Library on [18/11/2022]. See the Terms and Conditions (https://onlinelibrary.wiley.com/terms-and-conditions) on Wiley Online Library for rules of use; OA articles are governed by the applicable Creative Commons License

19447973, 2022, 8, Downloaded from https://agupubs.onlinelibrary.wiley.com/doi/10.1029/2021WR030680 by Cochrane France, Wiley Online Library on [18/11/2022]. See the Terms and Conditions (https://onlinelibrary.wiley.com/terms-and-conditions) on Wiley Online Library for rules of use; OA articles are governed by the applicable Creative Commons License

variations of Love waves as a function of water content. This fluid substitution approach makes sense here since the medium is very high in both porosity and permeability. It strongly limits capillary effects that introduce non linear effects in velocity changes (Knight & Nolen-Hoeksema, 1990; Solazzi et al., 2021). Under this approach, velocities changes in the $S_w = 0$–$0.95$ range are attributed to changes in bulk density: an increase in water saturation is therefore associated to a linear decrease $S$ wave velocity. The behavior of $P$-wave velocity is more complex, with a linear decrease followed by an abrupt increase when water saturation increases. The Love waves velocity, which only depends on that of $S$ waves, linearly decreases with increasing water saturation. Considering a porosity of 35%, the observed remaining 2% of $\delta v/v$ would correspond to water content variations of about 30%–35%. In order to interpret these observations, it should be reminded that the sensitivity of Love waves, analyzed for the velocity variation computations, is dominant and constant between depths of 2 and 7 m in the frequency range used (Supplementary material, Figure S2 in Supporting Information S1). During the experiment, the water table fluctuates between 3 and 6 m. This confirms that the water table level changes should strongly affect velocity variations. During drainage phases, the saturation profile above the water table and the capillary fringe exhibits a decreasing trend. The shape and dynamics of this profile are mainly controlled by gravity, capillary effects and relative permeability decrease induced by decreasing saturation. This behavior should promote a delayed drainage flow in the unsaturated zone. The latter could be accentuated by double porosity effects if the material presents an heterogeneous pore microstructure (Moench, 2008). Consequently, the slow rate of seismic velocity change could be due to the slower decrease of the water content within the desaturated zone, compared to the rate of water table level change.

The enlarged hysteretic behavior observed on P95 piezometer can be explained by its location well inside the basin. In this place, one can assume that infiltration and drainage flows are almost vertical. The S20 piezometer is located outside the basin, few meters away from the dyke. In this place, the seismic signal most likely integrates the contribution of the dyke to the water flow and to local capillary effects. The distribution of water at this location is certainly more complex and 3D, as observed on seismic tomographies (Figure 9).

Based on the high-resolution dynamic maps, we also compare the water table evolution measured along a line of piezometers globally oriented North/West-South/East (*i.e.*, Figure 10a) and the spatial extraction of the results derived from seismic tomography maps, at 6 different monitoring times (Figure 11). At first sight, the two measurements have a similar trend in subfigures (a), (b), and (c) and both render a dome shape with different spatial resolutions, the seismic tomography providing more detailed information. On the other hand, there is no information provided by the seismic approach on the northwest edge of the transect (distance labeled 0 m), due to a lack of illumination.

The tomography reveals that the dome has steeper slopes than those obtained by interpolation of the piezometric levels and that the maximum of water content change is shifted of several tens of meters to the southeast compared to the information provided by the single piezometer P95 located within the basin. The last drainage stage is characterized by a gradual return of the water table level to its initial state, while seismic velocities decay much more slowly and less homogeneously in space. Indeed, edge effects visible at the location of dykes seem to persist while the drainage is more efficient in the center of the basin. Interestingly, the two dykes do not completely show the same behavior: the southern one seems to fill and drain more quickly. Again, this observation reinforces the possibility of an effect of water flow in both saturated and unsaturated conditions within the dyke.

### 5.3. Potential Applications for the Monitoring of Various Hydrological Systems

Although already studied at different scales by different authors as mentioned in the introduction, this study reinforces the idea that seismic noise interferometry proves to be a complementary tool to the intrusive observations classically used in hydrology (when they are possible).

Indeed, this method has the potential to bring new information with high spatial resolution while keeping a satisfactory temporal resolution. Unlike active methods, which require logistics that are difficult to overcome over the long term, such passive method is easy to implement for monitoring purposes. $I_s$ is even well suited in urban areas which can be complicated to instrument with classical geophysical methods due to anthropic noise. It can reach an unmatched sensitivity that can detect velocity variations of the order of 0.1% in some cases (Brenguier et al., 2008; Clements & Denolle, 2018). Although site dependent, the amplitude of these variations have theoretically the potential to provide quantitative information of water content changes through fluid substitution

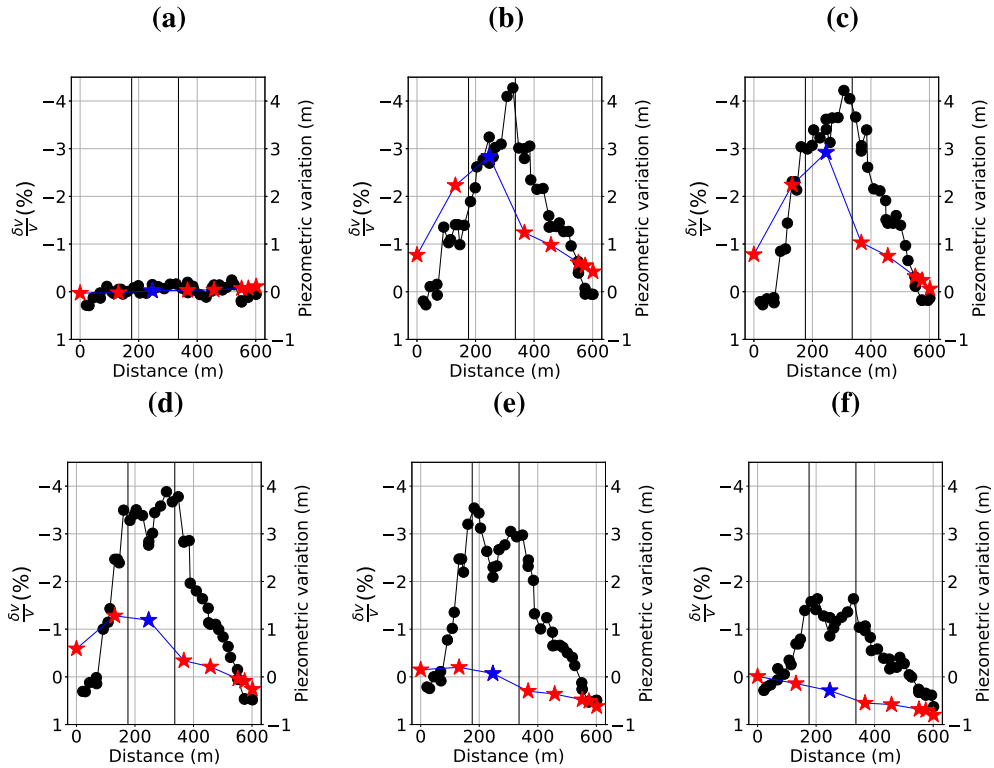



**Figure 11.** Comparisons between the relative water table variation measured on a line of piezometers and the corresponding velocity variations extracted from the (2–5 Hz) tomography maps obtained at (a) 60 hr, (b) 230 hr, (c) 385 hr, (d) 420 hr, (e) 440 hr, and (f) 456 hr. The stars represent the value of each piezometer along the transect (blue star highlights the P95 piezometer), while the black dots represent the value of the velocity variation obtained at each cell through the tomographies.

poroelastic type methods (Barrière et al., 2012; Garambois et al., 2019), while their frequency signatures gives the range of depth involved. To achieve this goal, controlled experiment performed at the site or laboratory scales would help assessing this seismic/hydrological relationship. Our study performed on controlled hydrological cycles shows significant variations of the order of a few percent, mainly because the recorded variations are integrated over shallow depths. It also shows an important sensitivity to water table changes but also to variations in water content within the unsaturated zone, making the response richer than piezometers but also more complex.

The measured velocity variations have a frequency signature that can theoretically provide water content variations in different depth ranges: the superficial variations should dominate at high frequencies while deeper variations should be accessible thanks to lower frequencies. It would be possible to quantify vertical transfers, provided that a sufficiently large frequency response and a model of velocity variations as a function of depth are available. In our case, the content of urban noise sources and the attenuation of sedimentary soils prevented us to benefit from a sufficiently broad spectrum. Moreover, the presence of a high-velocity layer that balances the sensitivities of the available frequencies between 2 and 7 m depth prevented us from constraining the infiltration and variations at depth. In natural systems, seismic noise imaging shows that it is possible to access a wider band frequency content, by combining anthropogenic and natural noise (Chmiel et al., 2019). Thus, it appears feasible to extend such study to follow, in 3D, deeper hydrological systems or more generally any process where natural or anthropogenic fluid transfers are involved. This can be done at large scale thanks to permanent seismological stations (Lecocq et al., 2017) or through transient installations at different scales depending on thestudied system (Clements & Denolle, 2018). In all cases, the spatial resolution will depend on the number of rays passing through a cell of the tomography grid, and consequently on the distribution and number of sensors.

For operational purposes, the feasibility of increasing the number of piezometers can be hindered by prohibitive drilling costs and environmental issues. The use of seismic interferometry with widely distributed sensors across water management sites can therefore offer a cheaper and non-intrusive alternative. As evidenced in this paper, the proposed methodology could offer an original spatialized information of the hydraulic func-



19447973, 2022, 8, Downloaded from https://agupubs.onlinelibrary.wiley.com/doi/10.1029/2021WR030680 by Cochrane France, Wiley Online Library on [18/11/2022]. See the Terms and Conditions (https://onlinelibrary.wiley.com/terms-and-conditions) on Wiley Online Library for rules of use; OA articles are governed by the applicable Creative Commons License

19447973, 2022, 8, Downloaded from https://agupubs.onlinelibrary.wiley.com/doi/10.1029/2021WR030680 by Cochrane France, Wiley Online Library on [18/11/2022]. See the Terms and Conditions (https://onlinelibrary.wiley.com/terms-and-conditions) on Wiley Online Library for rules of use; OA articles are governed by the applicable Creative Commons License

tioning of MAR basins. The same approach should be applicable to other MAR systems based on trenches or injection wells provided that the aquifer response is compatible with the sensitivity range of the method. In the framework of MAR systems using stormwater or wastewater, the dynamics of water flow within the unsaturated zone is identified as a key factor for contaminant removal. The ability of the method to provide informations on the drainage dynamics could probably be used to estimate residence times and thus a better understanding of the mechanisms related to the vadose zone. The seismic tomography strategy would provide valuable information about water exchanges at the larger scale of a drinking water pumping site or even a city where the sustainability of unconfined aquifers could rise concerns. To achieve this objective while maintaining a satisfactory spatial resolution, the number of seismic sensors in the acquisition network must be very dense, for instance through the use of distributed acoustic sensors (DAS). In this case, spatially continuous seismic information is provided by superficially buried optical fibers, or those already existing for communication purposes in urban areas, which can be interrogated regularly (Rodríguez Tribaldos & Ajo-Franklin, 2021).

## 6. Conclusions

This study proposes an assessment of the capacity of a dense seismic network operated passively to provide accurate information about the spatial and temporal evolution of the water table. The network was deployed around an infiltration basin located within a drinking water pumping site localized in an urban area. The role of this basin is: (a) to artificially recharge the aquifer to sustain the groundwater level and (b) to prevent the entry of polluted waters by reversing the water flow. The monitoring approach relies on the passive interferometry method, which consists of cross-correlating seismic noise recordings between pairs of stations, and precisely measuring their velocity variations. This experiment focused on the effect of two cycles of filling and drainage of the basin on the unconfined aquifer. We have demonstrated the sensitivity of the surface waves velocity to groundwater changes. The seismic velocity tends to decrease as the water content in the volume of interest increases. The proposed methodology well captured the water table rise due to the infiltration from the basin. However, during draw-down phases, the effect of delayed drainage appears to generate a hysteretic behavior of the $\delta v/v$ values with respect to the water table levels measured in control piezometers. This sensitivity to the behavior of the unsaturated zone opens very promising perspectives since available techniques mainly relies on local water content or suction sensors. Ongoing research aims at exploring this question based on laboratory scale controlled experiments.

The high density of the seismic network allowed applying a tomography approach, based on a high number of 4,851 seismic rays, to map the seismic signal with a high spatial resolution. Theses maps were computed on an hourly basis that appeared suitable to capture the dynamics of the studied phenomenon. Except computational and data storage costs, the time resolution of this procedure could reach 1–10 min, depending on the ray length, but at the risk of generating noisier time variations. As a first approximation, the seismic velocity variations are associated to the water table level changes. Seismic velocity variation maps thus provide coherent patterns of the hydraulic dome generated by the basin during filling/drainage cycles. It constitutes a promising complementary approach to piezometric maps interpolated from sparse data. Of note, it shows the high spatial variability of the dome with its strong asymmetry, which is crucial information to assess its effectiveness in terms of pollution prevention. We were also able to show that it is possible to detect residual variations within the unsaturated zone, above the piezometric water level. This study emphasizes the great potential of seismic noise interferometry for monitoring water table changes. Seismic networks at the water-field scale would be able to track groundwater and river exchanges, and the influence of pumping activities on the water resources, with outstanding resolution. This can be considered in the near future through the use of distributed acoustic measurement systems that can be deployed in a perennial way within this type of site, for a better management of water resources.

## Data Availability Statement

Seismological data can be accessed through the RESIF Seismological Data Portal https://seismology.resif.fr/networks/%23/1F%5F%5F2018. Piezometric and lake water height data and seismic metadata are available at the repertory users.isterre.fr/garambos/WRR2022/.

**Acknowledgments**
The authors thank Pierre Boué for providing a code for the beamforming computation; Aurelien Mordret for a checkerboard test used for tomography; Issam Seiffeidine (IGE) for access to the piezometric data; the "Plateforme de recherche de Crépieux-Charmy," particularly Gilles Régnier, for granting access and support for the experiments; the SIG service of ISTerre (Sandrine Roussel, Axel Jung, Ildut Pondaven). The instruments used in this study belong to the French national pool of portable seismic instruments SISMOB-RESIF (INSU-CNRS) and to the RESOLVE project (IRS-UGA). This work has been supported by a grant from Labex OSUG@2020 (ANR10 LABX56). The project leading to this publication has received funding from the Excellence Initiative of Université de Pau et des Pays de l'Adour – I-Site E2S UPPA. It benefited from the computing facilities of Pyrène UPPA.

## References

Barmin, M., Ritzwoller, M., & Levshin, A. (2001). A fast and reliable method for surface wave tomography. In *Monitoring the comprehensive nuclear-test-ban treaty: Surface waves* (pp. 1351–1375). Springer. https://doi.org/10.1007/978-3-0348-8264-4_3

Barrière, J., Bordes, C., Brito, D., Sénéchal, P., & Perroud, H. (2012). Laboratory monitoring of P waves in partially saturated sand. *Geophysical Journal International*, *191*(3), 1152–1170. https://doi.org/10.1111/j.1365-246X.2012.05691.x

Behr, Y., Townend, J., Bowen, M., Carter, L., Gorman, R., Brooks, L., & Bannister, S. (2013). Source directionality of ambient seismic noise inferred from three-component beamforming. *Journal of Geophysical Research: Solid Earth*, *118*(1), 240–248. https://doi.org/10.1029/2012jb009382

Binley, A., Hubbard, S. S., Huisman, J. A., Revil, A., Robinson, D. A., Singha, K., & Slater, L. D. (2015). The emergence of hydrogeophysics for improved understanding of subsurface processes over multiple scales. *Water Resources Research*, *51*(6), 3837–3866. https://doi.org/10.1002/2015wr017016

Boué, P., Roux, P., Campillo, M., & de Cacqueray, B. (2013). Double beamforming processing in a seismic prospecting context. *Geophysics*, *78*(3), V101–V108. https://doi.org/10.1190/geo2012-0364.1

Brenguier, F., Clarke, D., Aoki, Y., Shapiro, N. M., Campillo, M., & Ferrazzini, V. (2011). Monitoring volcanoes using seismic noise correlations. *Comptes Rendus Geoscience*, *343*(8–9), 633–638. https://doi.org/10.1016/j.crte.2010.12.010

Brenguier, F., Courbis, R., Mordret, A., Campman, X., Boué, P., Chmiel, M., et al. (2020). Noise-based ballistic wave passive seismic monitoring. Part 1: Body waves. *Geophysical Journal International*, *221*(1), 683–691. https://doi.org/10.1093/gji/ggz440

Brenguier, F., Shapiro, N., Campillo, M., Ferrazzini, v., Duputel, Z., Coutant, O., & Nercessian, A. (2008). Toward forecasting volcanic eruption using seismic noise. *Nature Geoscience*, *1*(2), 126–130. https://doi.org/10.1038/ngeo104

Campillo, M., & Paul, A. (2003). Long-range correlations in the diffuse seismic coda. *Science*, *299*(5606), 547–549. https://doi.org/10.1126/science.1078551

Chmiel, M., Mordret, A., Boué, P., Brenguier, F., Lecocq, T., Courbis, R., et al. (2019). Ambient noise multimode Rayleigh and Love wave tomography to determine the shear velocity structure above the Groningen gas field. *Geophysical Journal International*, *218*(3), 1781–1795. https://doi.org/10.1093/gji/ggz237

Clements, T., & Denolle, M. A. (2018). Tracking groundwater levels using the ambient seismic field. *Geophysical Research Letters*, *45*(13), 6459–6465. https://doi.org/10.1029/2018gl077706

Derode, A., Larose, E., Tanter, M., De Rosny, J., Tourin, A., Campillo, M., & Fink, M. (2003). Recovering the Green's function from field-field correlations in an open scattering medium (L). *Journal of the Acoustical Society of America*, *113*(6), 2973–2976. https://doi.org/10.1121/1.1570436

Garambois, S., Voisin, C., Romero Guzman, M., Brito, D., Guillier, B., & Réfloch, A. (2019). Analysis of ballistic waves in seismic noise monitoring of water table variations in a water field site: Added value from numerical modelling to data understanding. *Geophysical Journal International*, *219*(3), 1636–1647. https://doi.org/10.1093/gji/ggz391

Grêt, A., Snieder, R., & Scales, J. (2006). Time-lapse monitoring of rock properties with coda wave interferometry. *Journal of Geophysical Research*, *111*(B3), B03305. https://doi.org/10.1029/2004jb003354

Grobbe, N., Mordret, A., Barde-Cabusson, S., Ellison, L., Lach, M., Seo, Y.-H., et al. (2021). A multi-hydrogeophysical study of a watershed at Kaiwi Coast (O'ahu, Hawaii), using seismic ambient noise surface wave tomography and self-potential data. *Water Resources Research*, *57*(4), e2020WR029057. https://doi.org/10.1029/2020wr029057

Harmon, N., Gerstoft, P., Rychert, C. A., Abers, G. A., Salas de La Cruz, M., & Fischer, K. M. (2008). Phase velocities from seismic noise using beamforming and cross correlation in Costa Rica and Nicaragua. *Geophysical Research Letters*, *35*(19), L19303. https://doi.org/10.1029/2008gl035387

Hubbard, S., & Rubin, Y. (2005). Introduction to hydrogeophysics. In *Hydrogeophysics* (pp. 3–21). Springer.

James, S., Knox, H., Abbott, R., Panning, M., & Screaton, E. (2019). Insights into permafrost and seasonal active-layer dynamics from ambient seismic noise monitoring. *Journal of Geophysical Research: Earth Surface*, *124*(7), 1798–1816. https://doi.org/10.1029/2019jf005051

Kim, D., & Lekic, V. (2019). Groundwater variations from autocorrelation and receiver functions. *Geophysical Research Letters*, *46*(23), 13722–13729. https://doi.org/10.1029/2019gl084719

Knight, R., & Nolen-Hoeksema, R. (1990). A laboratory study of the dependence of elastic wave velocities on pore scale fluid distribution. *Geophysical Research Letters*, *17*(10), 1529–1532. https://doi.org/10.1029/gl017i010p01529

Larose, E., Carrière, S., Voisin, C., Bottelin, P., Baillet, L., Guéguen, P., et al. (2015). Environmental seismology: What can we learn from ambient noise? *Journal of Applied Geophysics*, *116*, 62–74. https://doi.org/10.1016/j.jappgeo.2015.02.001

Lecocq, T., Longuevergne, L., Pedersen, H. A., Brenguier, F., & Stammler, K. (2017). Monitoring ground water storage at mesoscale using seismic noise: 30 years of continuous observation and thermo-elastic and hydrological modeling. *Scientific Reports*, *7*(1), 14241. https://doi.org/10.1038/s41598-017-14468-9

Lobkis, O. I., & Weaver, R. L. (2001). On the emergence of the Green's function in the correlations of a diffuse field. *Journal of the Acoustical Society of America*, *110*(6), 3011–3017. https://doi.org/10.1121/1.1417528

Loizeau, S. (2013). Amélioration de la compréhension des fonctionnements hydrodynamiques du champ captant de crépieux-charmy (Unpublished doctoral dissertation).

Machiwal, D., Jha, M. K., Singh, V. P., & Mohan, C. (2018). Assessment and mapping of groundwater vulnerability to pollution: Current status and challenges. *Earth-Science Reviews*, *185*, 901–927. https://doi.org/10.1016/j.earscirev.2018.08.009

Moench, A. F. (2008). Analytical and numerical analyses of an unconfined aquifer test considering unsaturated zone characteristics. *Water Resources Research*, *44*(6), W06409. https://doi.org/10.1029/2006wr005736

Mordret, A., Jolly, A., Duputel, Z., & Fournier, N. (2010). Monitoring of phreatic eruptions using interferometry on retrieved cross-correlation function from ambient seismic noise: Results from Mt. Ruapehu, New Zealand. *Journal of Volcanology and Geothermal Research*, *191*(1–2), 46–59. https://doi.org/10.1016/j.jvolgeores.2010.01.010

Mordret, A., Rivet, D., Landès, M., & Shapiro, N. (2014). Three-dimensional shear velocity anisotropic model of Piton de la Fournaise Volcano (La Réunion Island) from ambient seismic noise. *Journal of Geophysical Research: Solid Earth*, *120*(1), 406–427. https://doi.org/10.1002/2014JB011654

Réfloch, A. (2018). Compréhension expérimentale et numérique des chemins de l'eau sur l'ensemble du champ captant de la métropole de lyon (Unpublished doctoral dissertation).

Réfloch, A., Gaudet, J.-P., Oxarango, L., & Rossier, Y. (2017). Estimation of saturated hydraulic conductivity from ring infiltrometer test taking into account the surface moisture stain extension. *Journal of Hydrology and Hydromechanics*, *65*(3), 321–324. https://doi.org/10.1515/johh-2017-0019



19447973, 2022, 8, Downloaded from https://agupubs.onlinelibrary.wiley.com/doi/10.1029/2021WR030680 by Cochrane France, Wiley Online Library on [18/11/2022]. See the Terms and Conditions (https://onlinelibrary.wiley.com/terms-and-conditions) on Wiley Online Library for rules of use; OA articles are governed by the applicable Creative Commons License

Rodríguez Tribaldos, V., & Ajo-Franklin, J. (2021). Aquifer monitoring using ambient seismic noise recorded with distributed acoustic sensing (das) deployed on dark fiber. *Journal of Geophysical Research: Solid Earth*, *126*(4), e2020JB021004. https://doi.org/10.1029/2020JB021004

Rost, S., & Thomas, C. (2002). Array seismology: Methods and applications. *Reviews of Geophysics*, *40*(3), 2–1. https://doi.org/10.1029/2000rg000100

Roux, P. (2009). Passive seismic imaging with directive ambient noise: Application to surface waves and the San Andreas Fault in Parkfield, CA. *Geophysical Journal International*, *179*(1), 367–373. https://doi.org/10.1111/j.1365-246x.2009.04282.x

Roux, P., & Ben-Zion, Y. (2017). Rayleigh phase velocities in Southern California from beamforming short duration ambient noise. *Geophysical Journal International*, *211*(1), 450–454. https://doi.org/10.1093/gji/ggx316

Rubin, Y., & Hubbard, S. S. (2006). *Hydrogeophysics* (Vol. 50). Springer Science & Business Media.

Sens-Schönfelder, C., & Wegler, U. (2006). Passive image interferometry and seasonal variations of seismic velocities at Merapi Volcano, Indonesia. *Geophysical Research Letters*, *33*(21), L21302. https://doi.org/10.1029/2006gl027797

Shapiro, N. M., Campillo, M., Stehly, L., & Ritzwoller, M. H. (2005). High-resolution surface-wave tomography from ambient seismic noise. *Science*, *307*(5715), 1615–1618. https://doi.org/10.1126/science.1108339

Solazzi, S. G., Bodet, L., Holliger, K., & Jougnot, D. (2021). Surface-wave dispersion in partially saturated soils: The role of capillary forces. *Journal of Geophysical Research: Solid Earth*, *126*(12), e2021JB022074. https://doi.org/10.1029/2021jb022074

Takano, T., Brenguier, F., Campillo, M., Peltier, A., & Nishimura, T. (2020). Noise-based passive ballistic wave seismic monitoring on an active volcano. *Geophysical Journal International*, *220*(1), 501–507. https://doi.org/10.1093/gji/ggz466

Vereecken, H., Huisman, J., Bogena, H., Vanderborght, J., Vrugt, J., & Hopmans, J. (2008). On the value of soil moisture measurements in vadose zone hydrology: A review. *Water Resources Research*, *44*(4), W00D06. https://doi.org/10.1029/2008wr006829

Voisin, C., Garambois, S., Massey, C., & Brossier, R. (2016). Seismic noise monitoring of the water table in a deep-seated, slow-moving landslide. *Interpretation*, *4*(3), SJ67–SJ76. https://doi.org/10.1190/int-2016-0010.1

Voisin, C., Guzman, M., Réfloch, A., Taruselli, M., & Garambois, S. (2017). Groundwater monitoring with passive seismic interferometry. *Journal of Water Resource and Protection*, *9*(12), 1414–1427. https://doi.org/10.4236/jwarp.2017.912091

Wang, K., Lu, L., Maupin, V., Ding, Z., Zheng, C., & Zhong, S. (2020). Surface wave tomography of northeastern Tibetan plateau using beamforming of seismic noise at a dense array. *Journal of Geophysical Research: Solid Earth*, *125*(4), e2019JB018416. https://doi.org/10.1029/2019jb018416

Wegler, U., Nakahara, H., Sens-Schönfelder, C., Korn, M., & Shiomi, K. (2009). Sudden drop of seismic velocity after the 2004 Mw 6.6 mid-Niigata earthquake, Japan, observed with Passive Image Interferometry. *Journal of Geophysical Research*, *114*(B6), B06305. https://doi.org/10.1029/2008jb005869

Zhang, H., Xu, Y., & Kanyerere, T. (2020). A review of the managed aquifer recharge: Historical development, current situation and perspectives. *Physics and Chemistry of the Earth, Parts A/B/C*, *118*, 102887. https://doi.org/10.1016/j.pce.2020.102887

## References From the Supporting Information

Herrmann, R. (2013). Computer programs in seismology: An evolving tool for instruction and research. *Seismological Research Letters*, *84*(6), 1081–1088. https://doi.org/10.1785/0220110096

Wathelet, M., Jongmans, D., & Ohrnberger, M. (2004). Surface wave inversion using a direct search algorithm and its application to ambient vibration measurements. *Near Surface Geophysics*, *2*(4), 211–221. https://doi.org/10.3997/1873-0604.2004018



19447973, 2022, 8, Downloaded from https://agupubs.onlinelibrary.wiley.com/doi/10.1029/2021WR030680 by Cochrane France, Wiley Online Library on [18/11/2022]. See the Terms and Conditions (https://onlinelibrary.wiley.com/terms-and-conditions) on Wiley Online Library for rules of use; OA articles are governed by the applicable Creative Commons License